J. Fluid Mech. (2000), *vol.* 417, *pp.* 303–322. Printed in the United Kingdom

A linear stability analysis of tidally generated sand waves

By THEO GERKEMA†

Institute for Marine and Atmospheric Research, Utrecht University, PO Box 80005, 3508 TA Utrecht, The Netherlands

(Received 21 August 1997 and in revised form 10 April 2000)

A linear stability analysis is carried out to examine the initial stage of sand-wave growth under tidal flows and the occurrence of a preferred length scale. The fact that these bedforms typically have length scales small compared to the tidal excursion is exploited by adopting an asymptotic approach to solve the hydrodynamic part of the problem, i.e. to find the hydrodynamic response to an initially small bed perturbation. This method is shown to have important advantages over previously used methods, since it allows an exploration of the complete sand-wave regime (whereas other methods fail for short sand waves), and in general it is also more accurate. It is found that the selection of a preferred length scale depends mainly on only two parameters (the bed-slope coefficient, and the ratio of friction velocity to eddy viscosity), whereas there appears to be almost no dependence on the water depth.

1. Introduction

In shallow seas like the North Sea various types of bottom patterns exist. Among them are the so-called *sand waves*, which have wavelengths of some hundreds of metres, amplitudes of several metres, and crests perpendicular to the principal tidal axis (e.g. Terwindt 1971; McCave 1971; Huntley *et al.* 1993). An example from the recent literature (O'Connor, Nunes & Sarmento 1996) is shown in figure 1. The observations raise several questions, such as why they appear at some places and not at others, what mechanisms account for their initial growth and later maintenance, and how to explain the remarkable regularity in the patterns. The first question is also of great practical relevance (navigation, off-shore industry, dredging activities).

One approach to deal with these questions is to use idealized models, with geometry and dynamics rendered in the simplest possible way, which do not aim at faithfully reproducing all observed features, but rather at increasing the insight into the basic mechanisms and the role of the various parameters in the system. This line of thought was followed in a series of recent studies (Hulscher, de Swart & de Vriend 1993; de Swart & Hulscher 1995; Hulscher 1996), in which the sand waves are conceived as an instability of the bed, due to the presence of an oscillating (tidal) flow. The idea behind this mechanism is that a wave-like perturbation of the bed, initially small, disturbs the tidal flow in a way that vertical residual cells are created. Near the bottom, the flow in these cells is directed from troughs to crests; in other words, the cells tend to move sediment from troughs to crests, i.e. to amplify the bed perturbation (thus providing a positive feedback mechanism). In addition to this, there is the opposite effect of the

† Present address: Netherlands Institute for Sea Research, PO Box 59, 1790 AB Den Burg, Texel, The Netherlands.

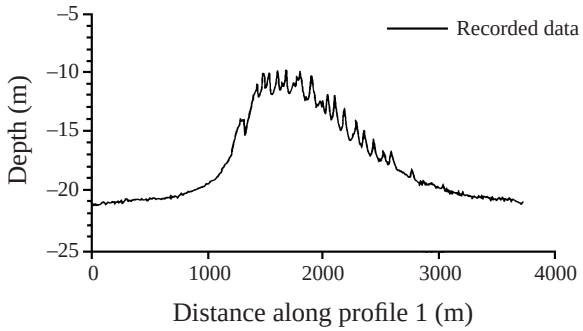

FIGURE 1. Observations on sand waves: measurements made along a section over Middelkerke Bank. (From: O'Connor *et al.* 1996.)

pull of gravity, which tends to move sediment downslope. The combination of these effects determines whether the bedform grows or decays. The growth rate depends on several parameters. Of particular importance is the dependence on the length scale of the bed perturbation: those with largest growth rate are expected to predominate in the natural sand-wave field.

The mechanism discussed above is qualitatively analogous to that in ripple formation under sea waves (Blondeaux 1990); however, the instability characteristics are very different, see § 6 below or Gerkema (1998). More remote is the analogy with the generation of dunes (and ripples) by a stationary flow, for which a linear stability analysis was carried out by Richards (1980). This will be discussed further in § 6; one difference is that for oscillatory (tidal) flows an additional parameter appears:

$$r = \frac{\text{tidal excursion amplitude}}{\text{topographic length scale}},$$

which plays an important role in the stability analysis of sand waves. For sand waves, r is large, since the tidal excursion (order 10 km) is much larger than the length scale of sand waves (order 100 m).

This paper aims to extend the analysis by Hulscher (1996) in two respects: first, by presenting alternative methods of solution, and second, by further investigating the dependence of the preferred length scale of the sand waves on the parameters in the system. Hulscher (1996) used a method (harmonic truncation) which basically assumes that r is small; there is no (*a priori*) reason why it should work also for large r (sand waves). Furthermore, the method becomes (numerically) intractable for short sand waves. In this paper an asymptotic method, similar to those applied to the Orr–Sommerfeld equation (Lin 1967; Drazin & Reid 1981), will be used which exploits the fact that r is large (§ 3.1). This asymptotic method is therefore very suitable for investigating sand waves, can be used to assess the validity of the method of harmonic truncation, and also allows a complete exploration of the sand-wave regime (including the short waves). Besides this asymptotic method, another method using power series will be presented (§ 3.2), which provides an easier and more direct way to obtain accurate solutions (except for short sand waves).

Hulscher (1996) made a classification of the preferred length scale in terms of the Stokes number and slip parameter. In this paper the effect of other parameters like the tidal current amplitude, the bed-slope coefficient, and the water depth will be investigated as well. In particular, the role of the last parameter will be shown to

mark a deviation from the properties of dunes in stationary flows (§ 6), implying that the sand waves are physically distinct from dunes.

The rest of this paper is organized as follows. In § 2 we start with the formulation of the governing equations, the basic state, the scaling and the perturbed equations. Then, in § 3, the hydrodynamic part of the problem is solved by the three methods discussed above, followed in § 4 by the morphodynamic part. In § 5 we present the main results: the stability properties of sand waves, the comparison of the three methods, and the role of the various parameters in the selection process of a preferred length scale. Finally, the main findings are summarized and discussed in § 6.

2. Formulation of the problem

We consider a two-dimensional system (three-dimensional, strictly, but with uniformity in the transverse direction, and no transverse flows). The flow is described by the momentum and continuity equation:

$$\boldsymbol{u}_t + (\boldsymbol{u} \cdot \nabla)\boldsymbol{u} = -\rho^{-1}\nabla p + A\nabla^2 \boldsymbol{u}, \tag{2.1}$$

$$\nabla \cdot \boldsymbol{u} = 0. \tag{2.2}$$

Here $\nabla = (\partial/\partial x, \partial/\partial z)$ and $\boldsymbol{u} = (u, w)$, where x and u (or z and w) denote the horizontal (or vertical) coordinate and velocity component, respectively. The density ρ and the eddy viscosity A are assumed to be constant. Coriolis effects are neglected, because the results of Hulscher (1996) indicate that these effects are not essential in the generation of sand waves.

The assumption of constant eddy viscosity is reasonable if the boundary conditions are adapted in a suitable way (Engelund 1970). This can be done by replacing the no-slip condition at the bottom by a partial-slip condition, which imposes a relationship between the bottom stress and the shear stress. The bottom stress itself can be written in terms of the flow velocity as $\tau = \rho C_d |u| u$ (C_d the drag coefficient), or in a simpler (linearized) form as $\tau = \rho v u$ (following Maas & van Haren 1987, we will refer to the quantity v as 'friction velocity'; it is proportional to the drag coefficient). Hence the partial-slip condition becomes $A u_z = v u$. It is convenient to introduce the stress parameter $\tilde{s} = v/A$, i.e. the friction velocity divided by eddy viscosity (note that it follows from the above that $\tilde{s}$ is proportional to the drag coefficient). The partial-slip condition was used or described by e.g. Prandle (1982), Bowden (1983), Maas & van Haren (1987); it provides an effective way of avoiding an analysis of the constant-stress layer (in which the flow profile is logarithmic), while retaining a way to calculate the stress at the bottom, which is one of the crucial quantities in morphodynamic studies (notice also that $\tilde{s}^{-1}$ can be interpreted as a measure of the constant-stress layer thickness). Representative parameter values are discussed in § 2.3.

We impose the following boundary conditions. At the bed, $z = \eta(t, x)$, the velocity component normal to the bed vanishes:

$$w = u\eta_x, \tag{2.3}$$

and the alongslope component, i.e. $u_\parallel = (u + \eta_x w)/(1 + \eta_x^2)^{1/2}$, satisfies the partial-slip condition

$$\frac{\partial}{\partial n} u_\parallel = \tilde{s} u_\parallel, \tag{2.4}$$

where $\partial/\partial n$ denotes the derivative in the normal direction, and $\tilde{s}$ the stress parameter

(if $\tilde{s}\to\infty$, infinite stress, no slip; if $\tilde{s}\to 0$, no stress, free slip). At the surface ($z = H$) we impose the conditions of no vertical velocity (rigid-lid) and no shear:

$$w, \quad u_z = 0. \tag{2.5}$$

(Free-surface gradients due to the tide can be neglected on the (much shorter) scale of sand waves; note that the rigid lid supports the pressure gradients that would otherwise have been caused by surface elevations on the sand-wave scale.)

The morphodynamic part consists of one single equation, which simply states that convergences (or divergences) of sediment flux must be accompanied by a rise (or fall) of the bed profile:

$$\eta_t + \langle Q\rangle_x = 0, \tag{2.6}$$

where the brackets indicate averaging over the period manifested on the short time scale (i.e. the tidal period), and Q denotes the sediment flux (divided by a porosity factor), which has to be parametrized in terms of the flow variables. A common choice for bed-load transport is (see e.g. Bailard & Inman 1981; Bailard 1981)

$$Q = \alpha|u|^3\left(\frac{u}{|u|} - \gamma\eta_x\right), \tag{2.7}$$

where α (order $10^{-4}\,\mathrm{s^2\,m^{-1}}$) and γ (between 1 and 3, the dimensionless bed-slope parameter) can be regarded as constants, apart from the fact that α is proportional to the drag coefficient (Bailard 1981); u is to be evaluated at some reference depth, e.g. at the top of the constant-stress layer. The first term on the right-hand side represents the forcing due to the flow over the bottom; the second term, the damping due to gravity (the sand grains are more easily transported downslope than upslope).

2.1. *The basic state*

As the basic state we take a unidirectional tidal flow ($u = u_b(t, z)$, $w = 0$) over a flat bottom; we assume that the flow is driven by a pressure gradient $p_x = -\rho P_0\cos\sigma t$ (P_0 is a constant; σ, the tidal frequency). The vertical momentum equation in (2.1), and (2.2), (2.3), (2.5*a*) and (2.6) are then trivially satisfied. The basic flow is solved from the horizontal momentum equation in (2.1), which reduces to

$$u_{b,t} = P_0\cos\sigma t + Au_{b,zz},$$

along with the boundary conditions (2.4) and (2.5*b*):

$$u_{b,z} = \tilde{s}u_b \text{ (at } z = 0), \quad u_{b,z} = 0 \text{ (at } z = H).$$

The solution u_b, which is given in Appendix A, has a rather complicated structure. It turns out, however, that for the purpose of this paper the basic state can be approximated by a much simpler profile, which is quadratic in z:

$$u_0 = U_0\,(z_c + z/H)(2 + z_c - z/H)\cos(\sigma t + \varphi), \tag{2.8}$$

where $z_c = -1 + (1 + 2/\tilde{s}H)^{1/2}$; U_0 and φ are fitting parameters. In general, close approximations can be obtained if $\mu(= H^2\sigma/A)$ is of order one, or smaller (examples are shown in Appendix A); the solutions become equal for $\mu\to 0$. Typical values for tidal currents in sand-wave fields are $\sigma = O(10^{-4}\,\mathrm{s^{-1}})$, $A = O(10^{-2}\,\mathrm{m^2\,s^{-1}})$ (see Bowden 1983) and depth $H = O(10\,\mathrm{m})$ (e.g. the sand-wave fields in the Southern North Sea). Hence $\mu = O(1)$, so we can use (2.8), which simplifies the rest of the analysis considerably.

2.2. *The perturbed state*

The next step is to perturb the basic state by introducing an infinitesimal topography of wavelength $2\pi/k$:

$$\eta = \Pi(t)\cos kx,$$

where Π describes the long-term evolution. The flow field now consists of two parts: the basic flow and the perturbed flow. It is convenient to write the latter in terms of a stream function:

$$(u, w) = (u_0, 0) + (\psi_z, -\psi_x).$$

The assumption that the topographic perturbation is infinitesimal implies that we are carrying out a *linear* stability analysis and that we can hereafter neglect all terms that involve products of either η or ψ, or both. Hence the stream function satisfies the linearized vorticity equation (which follows from (2.1)):

$$\nabla^2\psi_t + u_0\nabla^2\psi_x - \psi_x u_{0,zz} = A\nabla^4\psi, \tag{2.9}$$

where $\nabla^2 = \partial^2/\partial x^2 + \partial^2/\partial z^2$. In terms of ψ, the boundary conditions (2.3), (2.4) and (2.5) become after linearization

$$\psi_x + u_0\eta_x = 0, \quad \psi_{zz} + u_{0,zz}\eta = \tilde{s}(\psi_z + u_{0,z}\eta) \quad (\text{at } z = 0), \tag{2.10}$$

$$\psi_x, \quad \psi_{zz} = 0 \quad (\text{at } z = H). \tag{2.11}$$

In linearized form, (2.7) becomes

$$Q = \alpha u_0^3 + 3\alpha u_0^2\psi_z - \alpha\gamma|u_0|^3\eta_x. \tag{2.12}$$

The first term on the right-hand side is irrelevant (and will hereafter be ignored), because it gives no contribution in (2.6).

2.3. *Scaling*

The final preparatory step is to scale (2.9) to (2.12). We introduce the following scaled variables:

$$t' = \sigma t, \quad x' = kx, \quad z' = z/H, \quad u_0' = u_0/U_0, \quad \psi' = \psi/(U_0 H),$$

$$\eta' = \eta/H, \quad \Pi' = \Pi/H, \quad T' = t\alpha U_0^3/H^2, \quad Q' = Q/(\alpha U_0^3).$$

Here t' denotes the time variable related to the short time scale (tidal period), whereas T' is related to the long (morphodynamic) time scale. Using these scaled variables, we rewrite (2.9) in dimensionless form (dropping the primes):

$$\frac{1}{r}\nabla^2\psi_t + u_0\nabla^2\psi_x - \psi_x u_{0,zz} = \frac{1}{\mu r}\nabla^4\psi, \tag{2.13}$$

with $\nabla^2 = \delta^2\partial^2/\partial x^2 + \partial^2/\partial z^2$. The basic flow is now given by

$$u_0 = U(z)\cos t, \quad U(z) = (z_c + z)(2 + z_c - z), \quad z_c = -1 + (1 + 2/s)^{1/2}. \tag{2.14}$$

(The phase φ in (2.8) is removed by a translation in time).

Above, we used the following dimensionless parameters:

$$\delta = kH, \quad r = \frac{kU_0}{\sigma}, \quad \mu = \frac{H^2\sigma}{A}, \quad s = \tilde{s}H. \tag{2.15}$$

(The parameters E_v and $\hat{S}$ used in Hulscher 1996 are related to ours as follows: $E_v = 2/\mu$, $\hat{S} = 2s/\mu$.) In sand-wave fields typical depths are some tens of metres, so

the aspect ratio δ ranges roughly from 0.2 to 1. The second parameter denotes the ratio of the tidal excursion amplitude to the topographic length scale, and ranges from about 100 to 600; so always $r \gg 1$. The third parameter can be regarded as a reciprocal 'Stokes number' (roughly of order one in our case; take for instance the representative values $A = 0.01\,\mathrm{m^2\,s^{-1}}$, $H = 20\,\mathrm{m}$ and $\sigma = 0.0001\,\mathrm{s^{-1}}$, then $\mu = 4$). It is difficult to infer reliable estimates for the fourth parameter, s. An indication of its order of magnitude can be obtained from Maas & van Haren (1987), where $s \approx 10$ (for a depth of 48 m). As mentioned at the beginning of this section, the parameter $\tilde{s}A$ can be interpreted as a bottom friction velocity (Maas & van Haren 1987); a typical order of magnitude is $10^{-3}\,\mathrm{m\,s^{-1}}$.

In non-dimensional form, the boundary conditions (2.10) and (2.10) become

$$\psi_x + u_0\eta_x = 0, \quad \psi_{zz} + u_{0,zz}\eta = s(\psi_z + u_{0,z}\eta) \quad (\text{at } z = 0), \tag{2.16}$$

$$\psi_x,\ \psi_{zz} = 0 \quad (\text{at } z = 1), \tag{2.17}$$

where now

$$\eta = \Pi(T)\cos x. \tag{2.18}$$

Finally, (2.6) and (2.12) become

$$\eta_T + \delta\langle Q\rangle_x = 0, \tag{2.19}$$

$$Q = 3u_0^2\psi_z - \gamma\delta|u_0|^3\eta_x. \tag{2.20}$$

The rest of the analysis consists of two steps. First we have to find the *hydrodynamic* response to the topographic perturbation, that is, to solve ψ from (2.13), subject to the boundary conditions (2.16) and (2.17). Once ψ has been found, the *morphodynamic* response is readily obtained by substituting ψ in (2.20), and perform the averaging procedure over the tidal period in (2.19).

3. The hydrodynamic response

As discussed in the Introduction, we use three different methods for solving the vorticity equation, (2.13). First, the fact that a large parameter is involved (recall that $r \gg 1$ for sand waves), giving a small parameter in the viscosity term on the right-hand side, suggests the application of singular perturbation techniques (§ 3.1). In this construction, the first term of (2.13) plays no role. This suggests a second approach, in which we take the quasi-stationary version of (2.13) as a starting point, which is then solved in terms of a convergent power series in z without making any further approximations (§ 3.2). The numerical evaluation of the series becomes practically impossible for very large r (then the first method takes over), but for moderately large values it provides a valuable alternative to the asymptotic approach, because by comparing the two we can assess how large r should be for the asymptotic method to be reliable. The third method is the above-mentioned harmonic truncation (§ 3.3), which was used by Hulscher (1996). The results of the three methods will be compared in § 5.2.

3.1. *Asymptotic expansions*

In this subsection we derive first-order approximations to the vorticity equation, (2.13), by exploiting the fact that r is a large parameter. The methods we use here are described in detail by e.g. Lin (1967) and Drazin & Reid (1981) in their discussions on the Orr–Sommerfeld equation; without going into those details here, we provide only the main results that we need for the morphodynamic problem.

Hereafter we use alternatively the following transformed vertical coordinates:

$$\tilde{z} = z + z_c, \quad \xi = \tilde{z}/\epsilon,$$

in which ϵ is a small parameter which will turn out to be $\epsilon = r^{-1/3}$ (see below).

For large r, at leading order, the solution of (2.13) takes the following form:

$$\psi = \hat{\psi}_1(x, \tilde{z}; t) + \psi_2(x, \xi; t), \tag{3.1}$$

consisting of two parts, an inviscid ($\hat{\psi}_1$) and a viscous one (ψ_2).

The inviscid part is obtained if one assumes a balance between the advective terms in (2.13) (i.e. the terms that do not contain the small factor r^{-1}):

$$u_0 \nabla^2 \psi_x - \psi_x u_{0,\tilde{z}\tilde{z}} = 0. \tag{3.2}$$

Solutions can be constructed which are periodic in x, like (2.18), and depend parametrically on time:

$$\psi_1 = c_1(\phi_1 + \tilde{c}\phi_2)\cos x + c_2(\phi_1 + \tilde{c}\phi_2)\sin x, \tag{3.3}$$

in which

$$\phi_1(\tilde{z}) = \tilde{z}\sum_{n=0}^{\infty} d_n \tilde{z}^n, \quad \phi_2(\tilde{z}) = \frac{1}{b_0}\phi_1(\tilde{z})\log\tilde{z} + \frac{1}{b_0}\sum_{n=0}^{\infty} b_n \tilde{z}^n. \tag{3.4}$$

The constants b_n and d_n are given in Appendix B; c_1, c_2 and $\tilde{c}$ depend on time but are otherwise constant.

The inviscid balance (3.2) produces, via ϕ_2 in (3.4), a logarithmic singularity in ψ_1; this is an artefact resulting from a total neglect of the viscous terms. In fact, it can be removed by taking the viscous term on the right-hand side of (2.13) into account, giving a corrected expression $\hat{\phi}_2$ (which contains both a real and an imaginary part) instead of ϕ_2. This expression is derived by Drazin & Reid (1981, § 27.6) and tabulated by Stuart (1963, table IX.2), to which we refer for further details. The solution (3.3) is thus modified to an expression of the following form ('corrected inviscid solution'):

$$\begin{aligned}\hat{\psi}_1 = c_1 &\left([\phi_1(\tilde{z}) + \tilde{c}\,\mathrm{Re}(\hat{\phi}_2(\tilde{z}))]\cos x - \tilde{c}\,\mathrm{Im}(\hat{\phi}_2(\tilde{z}))\sin x\right) \\ &+ c_2\left([\phi_1(\tilde{z}) + \tilde{c}\,\mathrm{Re}(\hat{\phi}_2(\tilde{z}))]\sin x + \tilde{c}\,\mathrm{Im}(\hat{\phi}_2(\tilde{z}))\cos x\right).\end{aligned} \tag{3.5}$$

The correction plays a role in the lower part of the water column, while in the upper part $\mathrm{Re}(\hat{\phi}_2) \to \phi_2$ and $\mathrm{Im}(\hat{\phi}_2) \to 0$.

The other term in (3.1), the viscous part ψ_2, is obtained by first rescaling the vertical coordinate in (2.13), using ξ instead of $\tilde{z}$ (or z). Notice that for small $\tilde{z}$ (i.e. $\xi = O(1)$), the basic flow (2.14) can be approximated as

$$u_0 = \tilde{z}(C - \tilde{z})\cos t \approx \tilde{z}C\cos t = \epsilon\xi C\cos t \tag{3.6}$$

(where $C = 2(1+z_c)$) and thus gives an $O(\epsilon)$ contribution in the second term of (2.13). The four terms in (2.13) are then of order $r^{-1}\epsilon^{-2}$, ϵ^{-1}, 1, and $r^{-1}\epsilon^{-4}$, respectively. For small ϵ, the fourth term is much larger than the first term, and the second term much larger than the third; hence the dominant balance must be between the second and fourth terms, implying $\epsilon = r^{-1/3}$. At leading order, the viscous part ψ_2 must therefore satisfy

$$q(t)\xi\psi_{x\xi\xi} = \psi_{\xi\xi\xi\xi}, \tag{3.7}$$

with $q(t) = C\mu\cos t$. This, again, is analogous to the viscous balance in the Orr–

Sommerfeld equation (Drazin & Reid 1981, § 27.4) except for the (parametric) time-dependence which is present in (3.7). For $\cos t \geqslant 0$, the solution of this equation takes the following form

$$\psi_2 = c_3\left([\Lambda_1(\xi) + \gamma_1\xi + \gamma_2]\cos x - [\Lambda_2(\xi) + \gamma_3\xi + \gamma_4]\sin x\right) + c_4\left([\Lambda_1(\xi) + \gamma_1\xi + \gamma_2]\sin x + [\Lambda_2(\xi) + \gamma_3\xi + \gamma_4]\cos x\right), \quad (3.8)$$

where $\Lambda_{1,2}$ denote the series

$$\Lambda_1(\xi) = \xi^2 \sum_{n=0}^{\infty} \frac{a_n}{(n+1)(n+2)} (q^{1/3}\xi)^n \cos(n\pi/6), \quad (3.9)$$

$$\Lambda_2(\xi) = \xi^2 \sum_{n=0}^{\infty} \frac{a_n}{(n+1)(n+2)} (q^{1/3}\xi)^n \sin(n\pi/6). \quad (3.10)$$

(The coefficients a_n are given in Appendix B.) The solution for $\cos t < 0$ is simply obtained by replacing x with $-x$ in (3.8). In (3.8) additional terms are present in the form of $\gamma_1\xi$, $\gamma_3\xi$, γ_2 and γ_4; they are just lowest-order expressions of the inviscid solutions. Similar terms are implicitly present in (3.9) and (3.10). Since we include the inviscid solutions separately (via $\hat{\psi}_1$), we can ignore them here, and fix γ_1 to γ_4 such that in (3.8) the quantities between square brackets tend to zero for large ξ (the actual calculation of γ_1 to γ_4 is done numerically).

The expressions for $\hat{\psi}_1$ and ψ_2 being given by (3.5) and (3.8), respectively, we can apply the boundary conditions (2.16) and (2.17) to the solution (3.1) to obtain the (time-dependent) constants $\tilde{c}$ and c_i ($i = 1, \ldots, 4$).

By construction, $\psi \to \psi_1$ in the upper part of the water column; hence the conditions at the upper surface, (2.17), have to be applied to ψ_1, which is given by (3.3). Since ψ_1 is a solution of (3.2), it follows that if either of the boundary conditions in (2.17) is fulfilled, so is the other. Hence the application of (2.17) solves one constant (not two), namely

$$\tilde{c} = -\frac{\phi_1(1+z_c)}{\phi_2(1+z_c)}.$$

At the bed, each of the two conditions in (2.16) has to be applied to the $\cos x$ and $\sin x$ terms in (3.1), giving four equations in total for the remaining constants c_i ($i = 1, \ldots, 4$), which are solved numerically.

Finally, we make a few remarks on the time-dependence of $q(t)$ in (3.7), which makes the problem subtly different from the otherwise similar problem encountered in the Orr–Sommerfeld equation. First, since $q = C\mu\cos t$ is time-periodic, the viscous part of the solution (see (3.9) and (3.10)) contains, in principle, infinitely many higher harmonics. In practice, it suffices to include only the first 200 terms, say; including more gives no appreciable change in $\Lambda_{1,2}$. Second, it seems as if the whole asymptotic analysis breaks down if e.g. $t \approx \pi/2$, since then $q(t)$ approaches zero; this upsets the whole scaling. Indeed, one could argue that qr, rather than r, is the relevant parameter; strictly speaking, the asymptotic analysis is reliable only if qr is large. The problem is spurious, however, since the boundary conditions imply that for $\cos t$ small the constants c_1 to c_4 must be small, too. (This can be seen from the boundary conditions in (2.16): if $\cos t = 0$ then $u_0 = 0$ so that the forcing in (2.16) vanishes.) Hence during the interval at which t is close to $\pi/2$ the contribution to the net (i.e. tidally averaged) stress is negligible anyhow; in other words there are no significant *morpho*dynamic implications.

3.2. *A convergent power-series solution*

In this subsection we show that it is also possible to solve the hydrodynamic problem by writing the solution as a convergent power series, instead of using the above asymptotic approximations. To see how it works, consider the following equation:

$$\mathrm{i}\mu\cos t\Big(C\xi\partial_\xi^2-\xi^2\epsilon\partial_\xi^2-(\epsilon\delta)^2C\xi+\delta^2\epsilon^3\xi^2+2\epsilon\Big)\phi=(\partial_\xi^2-(\epsilon\delta)^2)^2\phi. \tag{3.11}$$

This equation follows from the vorticity equation (2.13) if we use the stretched coordinate $\xi=\tilde{z}/\epsilon$ (with $\epsilon=r^{-1/3}$), substitute $\psi=\phi\exp(\mathrm{i}x)$ (the real part being implied), and omit the $\partial/\partial t$ term. The last step, which is the only approximative step from (2.13) to (3.11), implies a quasi-stationary approach; this was shown to be legitimate in the regime $r\gg 1$ (see § 3.1). Note that (3.11) involves fewer approximations than the asymptotic approach of the previous subsection.

This fourth-order equation has analytic coefficients, which implies that it has an analytic solution. Hence we can write ϕ as a convergent power series in ξ (with an infinite radius of convergence). Despite its convergence, its practical evaluation is not always possible because very large ξ are involved. In the present problem, however, the evaluation appears to be feasible for values of r large enough to capture the long sand waves. The method thus provides a useful alternative to the asymptotic method, at least for part of the sand-wave regime.

We solve (3.11) by writing ϕ in terms of a double series:

$$\phi(\xi;t)=\sum_{k=1}^{8}\beta_k(t)\sum_{n=0}^{\infty}\alpha_{kn}(t)\xi^n, \tag{3.12}$$

with $\alpha=\alpha^R+\mathrm{i}\alpha^I$ ($\alpha^{R,I}$ real), and eight real β_k. Without loss of generality, we define, for $k=1,\ldots,8$ and $n=0,\ldots,3$:

$$\alpha_{kn}^R=1 \quad \text{if} \quad k=n+1,$$
$$\alpha_{kn}^I=1 \quad \text{if} \quad k=n+5,$$

and zero otherwise. To proceed, time must be discretized, and at each time step the problem is then solved as follows. Substitution of (3.12) in (3.11) yields recursion relations for $\alpha_{kn}^{R,I}$ which can be solved for $k=1,\ldots,8$ and $n\geqslant 4$ (in practice it suffices to stop at $n=200$, say); then the inner series in (3.12) can be evaluated. The only remaining unknowns are now the β_k; they follow by applying the boundary conditions (2.16) and (2.17), modified to the new coordinate ξ, to

$$\psi=\mathrm{Re}(\phi\exp(\mathrm{i}x))=\sum_{k=1}^{8}\beta_k\left\{\cos x\sum_{n=0}^{\infty}\alpha_{kn}^R\xi^n-\sin x\sum_{n=0}^{\infty}\alpha_{kn}^I\xi^n\right\}. \tag{3.13}$$

This involves (numerical) inversion of an 8×8 matrix.

3.3. *Method of harmonic truncation*

In this subsection we apply a method that was also used by Hulscher (1996); it is based on the assumption that the stream function can be represented by only a limited number of harmonics (the question of whether this assumption makes sense will be investigated in § 5.2). For example, if we truncate after the second harmonic:

$$\psi(t,x,z)=A(z)\sin x+B(z)\cos x\cos t+D(z)\cos x\sin t$$
$$+E(z)\sin x\cos 2t+F(z)\sin x\sin 2t. \tag{3.14}$$

The vorticity equation (2.13) is now solved by substituting (3.14). Notice that we include more harmonics than did Hulscher (1996), who ignored the double harmonics E and F. In § 5 we show that they can play a significant role in morphodynamic applications. For simplicity, in this part of the analysis we take the shallow-water limit (i.e. $\delta \to 0$), as did Hulscher (1996).

Substitution of (3.14) in (2.13) gives (denoting z derivatives by primes):

$$\mu^{-1}A'''' = -\tfrac{1}{2}rUB'' + \tfrac{1}{2}rU''B, \tag{3.15}$$

$$\mu^{-1}B'''' = D'' + rU(A'' + \tfrac{1}{2}E'') - rU''(A + \tfrac{1}{2}E), \tag{3.16}$$

$$\mu^{-1}D'''' = -B'' + \tfrac{1}{2}rUF'' - \tfrac{1}{2}rU''F, \tag{3.17}$$

$$\mu^{-1}E'''' = 2F'' - \tfrac{1}{2}rUB'' + \tfrac{1}{2}rU''B, \tag{3.18}$$

$$\mu^{-1}F'''' = -2E'' - \tfrac{1}{2}rUD'' + \tfrac{1}{2}rU''D. \tag{3.19}$$

Since U is polynomial (quadratic, see (2.14)), we can solve the set of coupled equations by writing A to F as power series in z (which converge for any value of z). As in the previous section, we write them as a double series, this time involving twenty constants $\beta_1, \ldots, \beta_{20}$. For example, A can be written

$$A(z) = \sum_{k=1}^{20} \beta_k \sum_{n=0}^{\infty} a_{kn} z^n. \tag{3.20}$$

Without loss of generality, we set, for $k = 1, \ldots, 20$ and $n = 0, \ldots, 3$,

$$a_{kn} = 1 \quad \text{if} \quad k = n + 1, \tag{3.21}$$

and zero otherwise. B to F are expressed similarly.

The coefficients a_{kn} (and b_{kn} etc.) can now be calculated for $k = 1, \ldots, 20$ and $n \geqslant 4$ (in practice it suffices to stop at $n = 150$) from five recursion relations, which are readily derived by substituting (3.20), along with the analogous expressions for B to F, into (3.15) to (3.19). The inner series in (3.20) can then be evaluated for any value of z. Finally, by applying the boundary conditions to (3.14), we obtain a set of twenty equations for β_1 to β_{20}, which can be solved numerically.

4. The morphodynamic response

Now that ψ has been obtained, we can calculate $\langle u_0^2 \psi_z \rangle$, which appears in the expression for $\langle Q \rangle$, the tidally averaged sediment flux, see (2.20). It appears that the only contribution comes from the $\sin x$ part in ψ; we can therefore write, in terms of a function θ,

$$3\langle u_0^2 \psi_z \rangle = -\Pi(T)\theta(z)\sin x. \tag{4.1}$$

Furthermore, we define $\theta_0 = \theta(0)$ and

$$\hat{\gamma} = \gamma \langle |U(0)\cos t|^3 \rangle = \frac{4}{3\pi}\gamma[z_c(2 + z_c)]^3. \tag{4.2}$$

Equation (2.19) can then be written as

$$\frac{\mathrm{d}\Pi}{\mathrm{d}T} + \delta(-\theta_0 + \hat{\gamma}\delta)\Pi = 0.$$

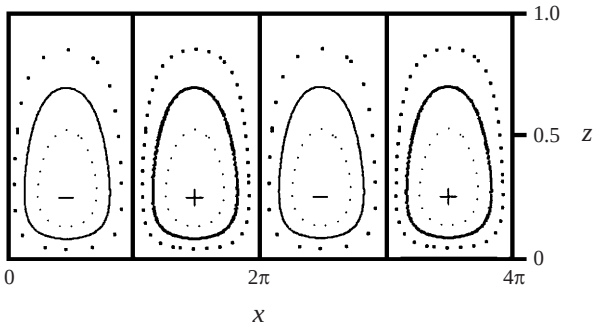

FIGURE 2. Contour plot of the residual (i.e. tidally averaged) stream function; in the lower part of the cells the flow is directed towards the crests. For parameter values, see text.

Substituting $\Pi = \exp(\omega T)$, we obtain the growth rate ω:

$$\omega = \delta(\theta_0 - \hat{\gamma}\delta). \tag{4.3}$$

It is convenient to introduce a *control parameter* Fo: $Fo = \hat{\gamma}^{-1}$, a measure of the forcing/damping ratio. The neutral stability curve is defined as the curve at which $\omega = 0$, and hence is obtained by plotting $Fo = \delta/\theta_0$ versus dimensional wavenumber k, or scaled wavenumber r.

5. Results

5.1. *Stability properties*

First we consider an example of the tidally averaged hydrodynamic response, which gives the vertical residual cells, see figure 2. The parameters chosen here (representative of sand-wave regions) are $k = 0.01\,\mathrm{m}^{-1}$, $H = 20\,\mathrm{m}$, $U_0 = 1\,\mathrm{m\,s}^{-1}$, $\sigma = 1 \times 10^{-4}\,\mathrm{s}^{-1}$, $A = 0.01\,\mathrm{m}^2\,\mathrm{s}^{-1}$, and $s = 10$, whence follows $\delta = 0.2$, $r = 100$, and $\mu = 4$. Here, the power series solution of § 3.2 was used; the other two methods give a very similar result. As expected, near the bottom the flow is directed towards the crests (the bottom being described by $\eta = \Pi(T)\cos x$); hence the flow tends to move sediment to the crests, and to amplify the sand wave; this effect is represented by the first term on the right-hand side of (4.3). An opposite tendency is effected by the downslope pull of gravity, represented by the second term on the right-hand side of (4.3). Which of the two is stronger depends on the various parameters, especially on wavenumber k. An instructive way of representing this k-dependence is by means of a stability curve.

An example is shown figure 3(a) (solid line), with the same parameter values as above, except of course that k (and hence δ and r, too) are now varied. Figure 3(a) is based on the asymptotic method described in § 3.1, including the viscous correction. Below the curve the perturbations decay ($\omega < 0$), above it they grow ($\omega > 0$). If the forcing is increased from zero onwards, the first waves to become unstable are not the sand waves ($r \approx 100$ to 600), but the ultralong ones ($r \to 0$); the implications of this are discussed in § 6.

In a sense, it is artificial to consider the change in stability properties with increasing forcing, since in practice one deals with some specific value of the forcing (i.e. $\hat{\gamma}^{-1}$). Another, and more relevant, way of representing the stability properties is therefore to consider in figure 3(a) how the growth rate varies along a transect at an appropriate level of the forcing; in other words to fix $\hat{\gamma}$ and plot the growth rate (4.3) versus r. For a representative value, $\gamma = 2$ (so that $\hat{\gamma}^{-1} \approx 147$), the result is shown in figure 3(b)

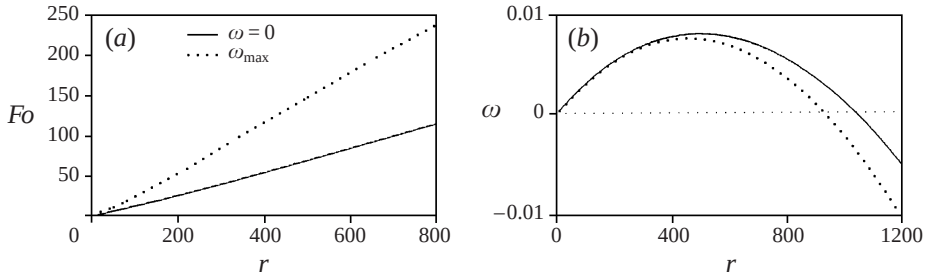

FIGURE 3. (*a*) The control parameter, $Fo = \hat{\gamma}^{-1}$, vs. scaled wavenumber r. The stability curve (solid line) indicates where in the forcing–wavenumber plane the growth rate vanishes; above the curve the growth rate is positive (the perturbation is unstable and grows), below the curve it is negative (the perturbation decays). The dotted line indicates where the growth rate takes its maximum. For parameter values, see text. The sand-wave regime extends from about $r = 100$ to 600; realistic values of the forcing are between 100 and 250. (*b*) The growth rate vs. scaled wavenumber r (solid line), according to equation (4.3). The maximum occurs for $r \approx 500$, which is in the sand-wave regime. The dotted line represents the case in which the hydrostatic approximation is made, and is discussed in § 5.2.

(solid line). Obviously, the maximum growth rate occurs within the sand-wave regime, namely for $r \approx 500$ (corresponding to a wavelength of about 126 m). This indicates that the present model is indeed pertinent to the analysis of sand-wave generation. Note that the growth rate tends to vanish for ultralong waves, and that it becomes negative for sufficiently short ones. Having found the maximum growth rate (0.008), we can also estimate the morphologic time scale, i.e. $[T]/\omega$ (cf. § 2.3); this gives the reasonable outcome of about 15 years.

Changes in the forcing ($\hat{\gamma}^{-1}$) result in a different value of r at which the growth rate takes its maximum; this can be visualized in the stability diagram, giving the dotted line in figure 3(*a*). It is significant that the dotted line maps the range of sand-wave wavenumbers ($r = 100$ to 600) fairly well onto the range of realistic values of the forcing (about 100 to 250, based on $\gamma = 1$ to 3).

5.2. *Comparison of the methods*

We now consider how the different methods used in § 3 compare with each other. In § 3.3 we applied the method of harmonic truncation along with the hydrostatic approximation, following Hulscher (1996). Note that the hydrostatic approximation amounts to setting $\delta = 0$ only in the hydrodynamic part of the analysis (§ 3), and not in the morphodynamic part; otherwise it would render for instance (4.3) completely useless. This in itself indicates that the hydrostatic approximation cannot be regarded entirely consistent in these and similar types of morphodynamic problems. However, in order to make a meaningful comparison between the three methods, we will for the moment apply the hydrostatic approximation also when using the other two methods (§ 3.1, § 3.2). (At the end of this subsection the hydrostatic approximation will be avoided in order to evaluate its quantitative effects.)

The parameters are now chosen as follows: $H = 20\,\mathrm{m}$, $U_0 = 1\,\mathrm{m\,s^{-1}}$, $\sigma = 1\times10^{-4}\,\mathrm{s^{-1}}$, $A = 0.04\,\mathrm{m^2\,s^{-1}}$ and $s = 5$; so $\mu = 1$. The reason for choosing A larger (μ smaller) and s smaller is that for the previously used values the maximum of the growth rate would occur beyond the range of wavenumbers that can be attained numerically with the methods of § 3.2 and § 3.3. Growth-rate plots are shown in figure 4 for the different methods: asymptotic approach with and without the viscous correction, the convergent power-series solution, and harmonic truncation with and without the

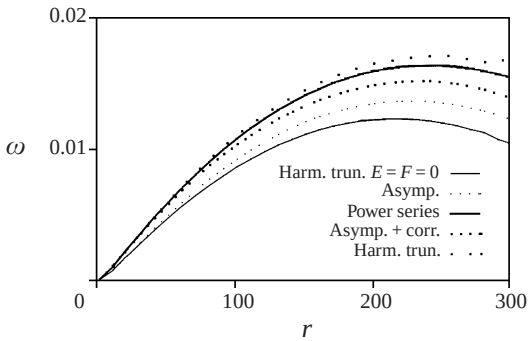

FIGURE 4. The growth rate vs. scaled wavenumber r, following five different methods. It can be argued that for large r the power-series solution should work best. Its curve is enclosed on one side by the solution that is based on small r (harmonic truncation) and on the other side by the solution that is based on large r (the asymptotic approach with correction). Harmonic truncation without the double harmonics E and F underestimates the value of r at which the growth is maximal, as well as the maximum growth rate itself.

double harmonics E and F in (3.14). No exact solution is available to compare with, but clearly the power-series method must be very accurate, particularly for the large values of r near maximum growth rates, because it only involves the assumption that the first term in (2.13) is negligible – a term which obviously is small for large r (in contrast to the right-hand side of (2.13), see the scaling and asymptotic procedure in § 3.1). In the asymptotic method (with or without correction) more terms are neglected, and hence it is plausibly less accurate. The difference between the most and least accurate solution (power-series and harmonic truncation with $E = F = 0$, respectively) in r at which the growth rate is maximal is about 13%; the difference in the maximum growth rate itself, about 28%. Inclusion of E and F in the method of harmonic truncation improves the result considerably; and so does inclusion of the viscous correction in the asymptotic approach (i.e. using $\hat{\psi}_1$ instead of ψ_1, see § 3.1). For values of r larger than about 300 the method of harmonic truncation and the power-series method begin to suffer from numerical inaccuracies in the evaluation of the series (some signs are already visible in figure 4). Beyond those values only the asymptotic approach can be used.

At first sight it seems paradoxical that the agreement between the power-series and the corrected asymptotic methods is not improved by increasing r, see figure 4. This is because for the latter to become more accurate it is not sufficient to increase r alone: s also has to be increased. For instance, in figure 4 the difference in growth rates is no smaller at $r = 300$ than at $r = 200$. But increasing s helps: at $r = 300$ the difference for $s = 5$ is 11%; for $s = 10$, 2%; and for $s = 20$, 0.2%.

We now turn to the regime of small r (which is outside the sand-wave regime), only to show that the method of harmonic truncation works better as r becomes smaller; in other words, the method is less well predisposed for application to sand waves (this provides the main motivation for the use of the alternative methods developed in this paper in § 3.1 and § 3.2). The differences between the methods are obvious from the different stability curves, see figure 5. The parameters are the same as for figure 4. The method of harmonic truncation becomes asymptotically correct for $r \to 0$. This can be seen as follows. For small r the solution of (2.13) can be written as an expansion in r; at order r^n one finds higher harmonics in time, up to the $n + 1$ harmonic. Harmonic truncation, then, is an immediate consequence of

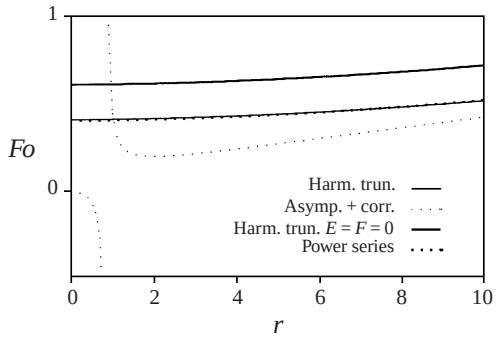

FIGURE 5. Stability curves in the regime of small r, following four different methods. Here, too, the power-series method works well; the curve almost coincides with that of harmonic truncation, the latter being asymptotically correct for $r \to 0$. Omitting E and F destroys the asymptotic correctness. The asymptotic method (with viscous correction), which is based on the assumption that r is large, is not reliable here.

truncating the expansion in r; hence the method of harmonic truncation works best as r approaches zero. Notice that at order r, both a time-independent term and double harmonics appear in the expansion; therefore, the solution without E and F in (3.14) gives incorrect results, asymptotically. The underlying reason is that θ in (4.1) indeed contains order-r contributions from both A and E. For a simpler parametrization of sediment transport, taking $|u|$ instead of $|u|^3$ in (2.7), the absence of E would have no harmful effects. Surprisingly, the power-series method also works well for small r, provided that μ is not too large. In fact, for $\mu \to 0$ and $r \to 0$ the method becomes equivalent to that of harmonic truncation. In accordance with one's expectations, the asymptotic method has no validity in the regime of small r, and gives absurd results.

Finally, we consider the effect of the hydrostatic approximation. A representative example is shown in figure 3(b) (hydrostatic approximation: dotted line). As expected, the difference between the curves becomes larger for larger r (shorter waves). The hydrostatic approximation leads to an underestimation of both the maximum growth rate and the wavenumber at which it occurs. So, if one uses (as in Hulscher 1996) (a) the method of harmonic truncation without double harmonics, and (b) the hydrostatic approximation, then the combined effect of each leads to a considerable underestimation, both in the maximum growth rate and in the corresponding wavenumber.

5.3. *Dependence on the parameters*

In this subsection we examine how the maximum growth rate ($\omega_{\max}$) and its corresponding value of r (referred to as $r_{\max}$) depend on the model parameters; we focus on H, U_0, γ, $\tilde{s}$ and A (for definitions, see § 2.3). In all cases discussed hereafter, the asymptotic method (with correction; non-hydrostatic) is used, because only this method allows an exploration of the complete sand-wave regime. The following parameter values are used (unless stated otherwise): $H = 20$ m, $U_0 = 1\,\mathrm{m\,s^{-1}}$, $\sigma = 1.4 \times 10^{-4}\,\mathrm{s^{-1}}$, $A = 0.01\,\mathrm{m^2\,s^{-1}}$, $\tilde{s} = 0.5\,\mathrm{m^{-1}}$ (hence $\tilde{s}A = 5 \times 10^{-3}\,\mathrm{m\,s^{-1}}$, being a 'friction velocity'), and $\gamma = 2$.

We start by varying the water depth, H. By changing H we change four parameters: δ (depth over length scale), μ (reciprocal Stokes number), s (stress parameter), and (via s and z_c) $\hat{\gamma}$, see (4.2). The dependence of $r_{\max}$ on water depth is shown in figure 6(a); remarkably, there appears to be none. This is possibly confirmed by a recent

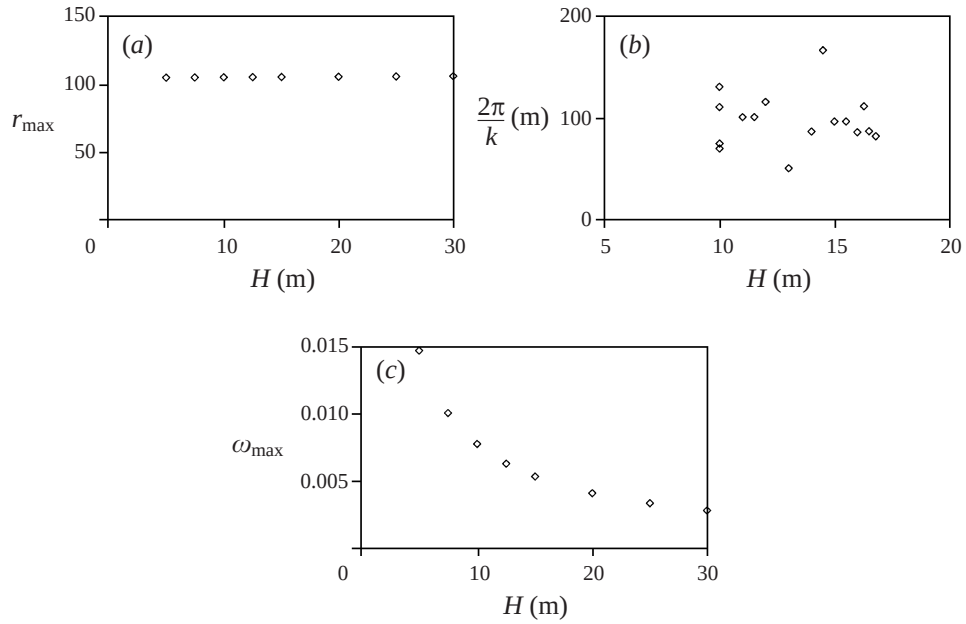

FIGURE 6. (*a*) The (scaled) wavenumber for which the growth rate is maximal, r_{max}, appears to be independent of water depth. (*b*) The wavelength of sand waves from observations across Middelkerke Bank vs. local water depth (O'Connor *et al.* 1996). This somewhat fuzzy scatter plot does not suggest a clear dependence on water depth, in accordance with (*a*). (*c*) The maximum growth rate, ω_{max}, decreases with increasing water depth.

observation (O'Connor *et al.* 1996), in which there is no clear indication pointing towards a dependence of wavelength on water depth, see figure 6(*b*).

The behaviour of ω_{max} against H is shown in figure 6(*c*): the growth rate decreases with increasing water depth. Notice, however, that the dimensional growth rate (i.e. $\omega/[T]$) decreases even faster, because $[T] \sim H^2$, see § 2.3.

Next we vary the amplitude of the tidal flow, U_0. The dependence of k_{max} on U_0 appears to be weak, see figure 7(*a*): the length scale increases only slightly for stronger flows. The dimensionless growth rate decreases slowly with increasing U_0 (not shown), suggesting an increase in the morphologic time scale. This effect, however, is spurious, since it is reversed when we consider the *dimensional* growth rate, which increases rapidly with increasing U_0, as one would indeed expect (the reason is that the denominator of $[T]$ contains a factor U_0^3, see § 2.3).

The dependence on the bed-slope parameter, γ, was already partly discussed in § 5.1, see figure 3(*a*), which indicates that k_{max} is approximately inversely proportional to γ; and so then is ω_{max}, as follows from (4.3). In other words, a larger bed-slope coefficient gives longer sand waves with smaller growth rates.

Finally, we consider the influences of the friction velocity (i.e. $\tilde{s}A$) and the eddy viscosity (A). There are essentially three ways to proceed: first, to vary $\tilde{s}$ while keeping A constant; second, to vary A while keeping $\tilde{s}$ constant; third, to vary both A and $\tilde{s}$ such that $\tilde{s}A$ remains constant.

The first case amounts to varying only the friction velocity (i.e. $\tilde{s}A$, with $\tilde{s}$ varied and A fixed); hence the stress parameter s is varied whereas the other parameters in (2.15) remain constant. The result is shown in figure 7(*b*), which attests to a strong dependence of the preferred length scale on the stress parameter: stronger friction

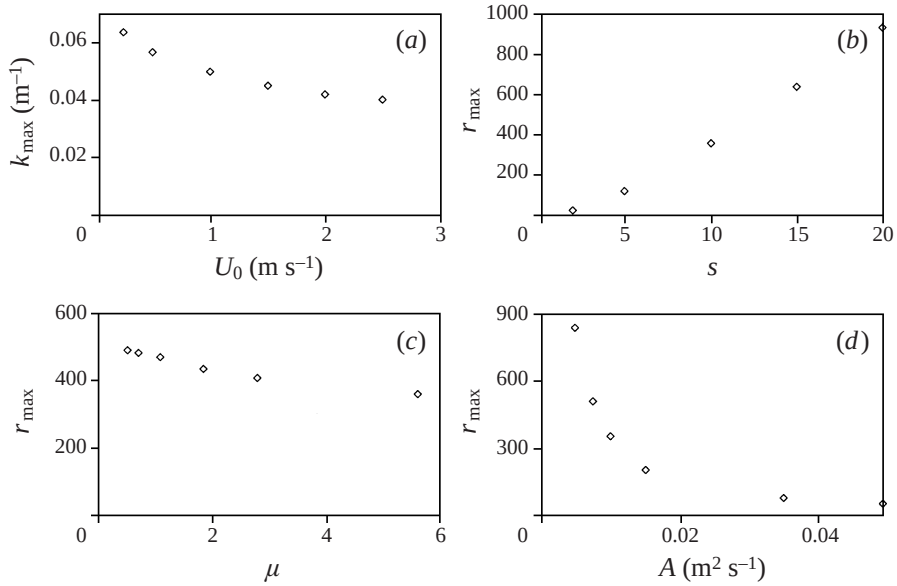

FIGURE 7. (*a*) The wavenumber for which the growth rate is maximal, k_{max}, depends only weakly on the amplitude of the tidal current, U_0. (*b*) The (scaled) wavenumber for which the growth rate is maximal, r_{max}, depends strongly on the stress parameter s, which is here varied by varying the friction velocity while keeping the eddy viscosity constant. (*c*) The (scaled) wavenumber for which the growth rate is maximal, r_{max}, depends only weakly on the eddy viscosity A if the friction velocity is varied at the same rate as the eddy viscosity. Thus μ is varied, whereas s remains constant. (*d*) The (scaled) wavenumber for which the growth rate is maximal, r_{max}, depends strongly on the eddy viscosity A if the friction velocity is kept fixed. Thus both μ and s are varied.

gives smaller length scales. The dimensionless growth rate ω_{max} decreases too (not shown), but this tendency is reversed in the dimensional growth rate, which contains (via α) a drag coefficient that can be assumed proportional to the friction velocity (as discussed at the beginning of § 2), and thus increases with increasing s. For larger values of s we thus find larger r_{max} and shorter dimensional morphologic time scales.

The second case implies that we vary both the friction velocity ($\tilde{s}A$) and the eddy viscosity (A), while keeping their ratio ($\tilde{s}$) constant. Hence μ is varied, whereas the other parameters in (2.15), in particular s, remain fixed. The result is shown in figure 7(*c*). Although there is a clear dependence, it is much less pronounced than in the previous case. The maximum growth rate ω_{max} decreases weakly with increasing μ (in this case the trend is not reversed when considering the dimensional growth rate; on the contrary, as μ increases, A and hence the friction velocity decrease, yielding a smaller factor in the dimensional growth rate).

In the third case we keep the friction velocity ($\tilde{s}A$) constant (see the reference value above) while varying the eddy viscosity A. This implies that now both μ and s (via $\tilde{s}$) are varied. As in the first case, a strong dependence is found, see figure 7(*d*): larger A gives longer sand waves. The dimensionless growth rate increases with increasing A (not shown), but, as in the first case, the corresponding decrease in the stress parameter s gives an additional factor in the dimensional growth rate, which reverses the trend.

The conclusion to be drawn from the last three cases is that r_{max} depends chiefly on the ratio of the friction velocity and the eddy viscosity, i.e. $\tilde{s}$, rather than on each

of the two separately. (In the notation of Hulscher 1996 this means that the main dependence is on the ratio $\hat{S}/E_v$.)

6. Conclusion

The most complicated step in analysing the morphodynamic instabilities appears to be the solution of the hydrodynamic problem (vorticity equation), i.e. to examine how the flow responds to a bed perturbation. In this analysis we solved the vorticity equation in three different ways: (i) using asymptotic methods; (ii) using a power-series solution of the quasi-steady vorticity equation; (iii) using harmonic truncation.

The first method is based on the assumptions that r, the ratio of tidal excursion to topographic length scale, is large (which is the case for sand waves), and also that the stress parameter s is sufficiently large. No assumption about s is made in the second method, only r needs be large. The third method works best for small r, but was here shown still to give reasonable results for relatively large values of r. The merit of the first method is that it works in all practical cases, whereas the second and third methods break down for short sand waves. Hence only the first method, which was not used earlier in studies on sand-wave generation, allows a complete exploration of the sand-wave regime.

All three methods as they are used here involve the assumption that μ (reciprocal Stokes number) must be sufficiently small (order one or less, say) to justify the simplification of the basic state.

The stability properties of sand waves appear to be crucially different from those of sand ripples, as studied by Blondeaux (1990). In that study it was found that for increasing forcing the first waves to become unstable are within the ripple regime; in other words the stability curve has a minimum in that regime. By contrast, in the present sand-wave study, the first waves to become unstable are in the ultralong regime; the stability curve is now monotonically increasing. It was shown by Gerkema (1998) that the difference in long-wave stability between the ripple and the sand-wave case is essentially due to the very different values of the Stokes parameter. Whereas we have $\mu = O(1)$, in the ripple case studied by Blondeaux (1990) an infinitely thin Stokes layer was assumed, hence $\mu \to \infty$. So, despite the various analogies between the two cases, there is an essential difference, too.

The morphodynamic implications are as follows. First, since there is no wave-number k in the sand-wave regime which corresponds to a minimum of the stability curve, the present analysis does not provide a starting point for a weakly nonlinear analysis (in which case one assumes that the forcing is only slightly stronger than the critical forcing; this leads to the Ginzburg–Landau type of equations, see e.g. Dodd *et al.* 1982; Nicolis 1995). Second, for realistic parameters the growth rate takes its maximum within the sand-wave regime. Thus a preferred length scale is found, which explains why certain length scales are predominant in nature.

The selection of a preferred length scale appears to be determined mainly by two parameters: the bed-slope coefficient $\hat{\gamma}$, and the ratio of friction velocity to eddy viscosity, here termed $\tilde{s}$ (which is contained in the stress parameter s). The latter dependence is particularly interesting, because in a wider context (in which tidal ridges were also considered) Hulscher (1996) found that the type of dominant bedform was determined by the friction velocity and the eddy viscosity separately. In now appears, then, that within the sand-wave regime a reduction in parameter space takes place, in that their ratio becomes a determining parameter, rather than each separately. Furthermore, the results of § 5.3 yield the surprising conclusion that neither the water

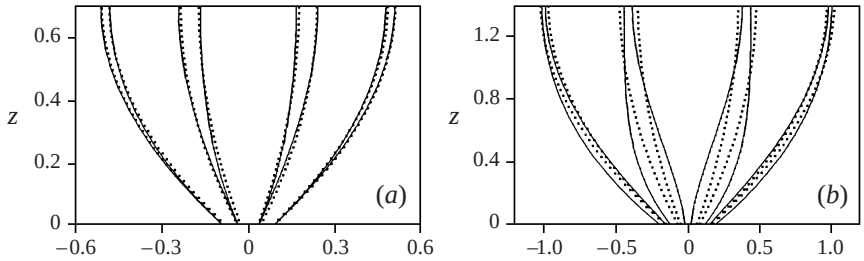

FIGURE 8. Comparison of the exact basic state u_b (lines) with the approximation u_0 (dots), at eight different phases during a tidal period, for $s = 10$. In (*a*) $\mu = 1$; in (*b*) $\mu = 4$.

depth nor the strength of the tidal flow plays a significant role in the selection of the preferred length scale (although they are of course important to the growth rate, i.e. the morphologic time scale). This makes the problem essentially different from the analysis of bed instabilities in a *stationary* flow (Richards 1980), since the 'dune-mode' found there depends strongly on water depth. The difference may be partly due to the difference in modelling turbulence (Richards used a closure scheme with turbulent kinetic energy), but it more likely indicates that there is only a weak analogy between bedforms generated by a stationary flow and those generated by a tidal flow. (Also, Richards' analysis yielded a second, ripple mode, but the absence of an analogue in the present analysis is not surprising because, as Richards notes, that mode does not appear in a model with constant eddy viscosity.)

The work presented here suggests some natural sequels, such as to include a stationary component in the basic state (which may explain the migration of sand waves, their asymmetry, and the appearance of mega-ripples on their flanks), and to use a more sophisticated formulation of the basic state (e.g. by omitting the partial-slip construction).

The author would like to acknowledge the useful discussions on this topic with Dr Huib de Swart. This work was financially supported by GOA (Geosciences Foundation) of the Netherlands Organization for Scientific Research (contract 750-29-405), and by the Netherlands Centre for Coastal Research (NCK).

Appendix A. Basic flow

This Appendix contains some technical details on the approximation of the basic state (§ 2.1). The exact solution of the basic state u_b (referred to, but not given, in § 2.1) reads

$$u_b(t,z) = \frac{P_0}{\sigma}\left[\sin\sigma t - \mathrm{e}^{-\beta z}\sin(\sigma t - \beta z)\right.$$
$$-\cos\sigma t\{p_1\cos\beta z\sinh\beta z + p_2\sin\beta z\cosh\beta z + p_3\cos\beta z\cosh\beta z + p_4\sin\beta z\sinh\beta z\}$$
$$\left.-\sin\sigma t\{p_2\cos\beta z\sinh\beta z - p_1\sin\beta z\cosh\beta z + p_4\cos\beta z\cosh\beta z - p_3\sin\beta z\sinh\beta z\}\right],$$

where $\beta^2 = \sigma/2A$. The constants p_1 to p_4 follow from the boundary conditions and are easily obtained (numerically). Two comparisons with the approximation (2.8) are shown in figure 8(*a*, *b*). For convenience, z was scaled with β^{-1} and t with σ^{-1}, and the amplitude factor P_0/σ was omitted. As discussed above, the approximation becomes exact as $\mu \to 0$. For $\mu = 1$ (with fitting amplitude 0.9 and $\phi = -0.46$) the agreement

is excellent, while for $\mu = 4$ (with fitting amplitude 0.45 and $\phi = 5.17$) it is worse, but still acceptable for the purpose of this paper.

Appendix B. Coefficients

In the asymptotic method (§ 3.1) various coefficients appear. The explicit expressions follow below. Those of the inviscid solutions, (3.4), are given by

$$d_0 = 1, \quad d_1 = -d_0/C, \quad d_2 = \delta^2 d_0/6,$$

$$d_{n+1} = \frac{[n(n+1)-2]d_n + C\delta^2 d_{n-1} - \delta^2 d_{n-2}}{(n+1)(n+2)C} \quad (n \geqslant 2),$$

where $C = 2(1+z_c)$; we fixed d_0 (which can be chosen arbitrarily) by making the conventional choice. The inviscid solution also contains

$$b_0 = -\tfrac{1}{2}Cd_0, \quad b_1 = 0, \quad b_2 = \tfrac{1}{2}(\delta^2 b_0 + d_0/C - 3d_1),$$

$$b_{n+1} = \frac{[n(n-1)-2]b_n + \delta^2(Cb_{n-1} - b_{n-2}) - (2n+1)Cd_n + (2n-1)d_{n-1}}{n(n+1)C} \quad (n \geqslant 2).$$

In this case b_1 is arbitrary.

The coefficients in the viscous solution (3.9) and (3.10) are given by

$$a_0 = 3^{-2/3}/\Gamma(2/3), \quad a_1 = -3^{-4/3}/\Gamma(4/3), \quad a_2 = 0, \quad a_n = \frac{a_{n-3}}{n(n-1)} \quad (n \geqslant 3),$$

where a_0 and a_1 are the conventional choices for the Airy function Ai (to which $\Lambda_{1,2}$ are related); Γ denotes the gamma-function.

REFERENCES

Bailard, J. A. 1981 An energetics total load sediment transport model for a plane sloping beach. *J. Geophys. Res.* **86** (C11), 10938–10954.

Bailard, J. A. & Inman, D. L. 1981 An energetics bedload model for a plane sloping beach: local transport. *J. Geophys. Res.* **86** (C3), 2035–2043.

Bender, C. M. & Orszag, S. A. 1978 *Advanced Mathematical Methods for Scientists and Engineers.* McGraw-Hill.

Blondeaux, P. 1990 Sand ripples under sea waves. Part 1. Ripple formation. *J. Fluid Mech.* **218**, 1–17.

Blondeaux, P. & Vittori, G. 1994 Wall imperfections as a triggering mechanism for Stokes-layer transition. *J. Fluid Mech.* **264**, 107–135.

Bowden, K. F. 1983 *Physical Oceanography of Coastal Waters.* Ellis Horwood.

Dodd, R. K., Eilbeck, J. C., Gibbon, J. D. & Morris, H. C. 1982 *Solitons and Nonlinear Wave Equations.* Academic.

Drazin, P. G. & Reid, W. H. 1981 *Hydrodynamic Stability*. Cambridge University Press.

Engelund, F. 1970 Instability of erodible beds. *J. Fluid Mech.* **42**, 225–244.

Gerkema, T. 1998 A note on the effect of finite Stokes-layer thickness in a morphodynamic stability problem. In *Proc. 8th Intl Biennial Conf. on Physics of Estuaries and Coastal Seas* (ed. J. Dronkers & M. Scheffers), pp. 387–395. Balkema.

Hulscher, S. J. M. H. 1996 Tidal-induced large-scale regular bed form patterns in a three-dimensional shallow water model. *J. Geophys. Res.* **101** (C9), 20727–20744.

Hulscher, S. J. M. H., Swart, H. E. de & Vriend, H. J. de 1993 Generation of offshore tidal sand banks and sand waves. *Cont. Shelf Res.* **13**, 1183–1204.

Huntley, D. A., Huthnance, J. M., Collins, M. B., Liu, C. L., Nicholls, R. J. & Hewitson, C. 1993 Hydrodynamics and sediment dynamics of North Sea sand waves and sand banks. *Phil. Trans. R. Soc. Lond.* A **343**, 461–474.

Lin, C. C. 1967 *The Theory of Hydrodynamic Stability*. Cambridge University Press.

Maas, L. R. M. & Haren, J. J. M. van 1987 Observations on the vertical structure of tidal and inertial currents in the central North Sea. *J. Mar. Res.* **45**, 293–318.

McCave, I. N. 1971 Sand waves in the North Sea off the coast of Holland. *Marine Geol.* **10**, 199–225.

Nicolis, G. 1995 *Introduction to Nonlinear Science*. Cambridge University Press.

O'Connor, B. A., Nunes, C. R. & Sarmento, A. J. N. A. 1996 Sand wave dimensions and statistics. In *CSTAB Handbook and Final Report* (ed. B. A. O'Connor), pp. 336–353. University of Liverpool.

Prandle, D. 1982 The vertical structure of tidal currents and other oscillatory flows. *Cont. Shelf Res.* **1**, 191–207.

Richards, K. J. 1980 The formation of ripples and dunes on an erodible bed. *J. Fluid Mech.* **99**, 597–618.

Stuart, J. T. 1963 Hydrodynamic stability. In *Laminar Boundary Layers* (ed. L. Rosenhead), pp. 492–579. Oxford University Press.

Swart, H. E. de & Hulscher, S. J. M. H. 1995 Dynamics of large-scale bed forms in coastal seas. In *Nonlinear Dynamics and Pattern Formation in the Natural Environment* (ed. A. Doelman & A. van Harten), pp. 315–331. Longman.

Terwindt, J. H. J. 1971 Sand waves in the Southern Bight of the North Sea. *Mar. Geol.* **10**, 51–67.